CONEM 2022
CONGRESSO NACIONAL DE ENGENHARIA MECÂNICA
TERESINA - PI

ABCM

XI CONGRESSO NACIONAL DE ENGENHARIA MECÂNICA
DE 07 A 11 DE AGOSTO DE 2022, TERESINA-PI, BRASIL

DYNAMICAL ANALYSIS OF A FERROFLUID IN MAGNETIC HYPERTHERMIA

Filipe Eduard Leite Ossege, eduard.ossege@gmail.com[1]
Aline Souza de Paula, alinedepaula@unb.br[1]
Rafael Gabler Gontijo, rafael.gabler@unb.br[1]

[1]Universidade de Brasília, 70.910-900, Brasília, DF

Abstract: *Magnetic hyperthermia is a cancer treatment which aims the growth of the tumor's temperature, by means of applying magnetic particles in an organic unhealthy tissue under magnetic field. With the development of nanotechnology, this medical procedure became feasible and more investigated among scientists. However, the nonlinear dynamics of the magnetic fluid responsible for the hyperthermia have not yet been considered by the literature. Hence, the main contribution of this work is the analysis of the problem in a dynamical point of view. In this way, the main objective of this work is the characterization of the dynamical behavior of magnetic particles, that consists of the ferrofluid used in magnetic hyperthermia. To do so, a numerical methodology is considered, where magnetic particles immersed in a liquid carrier are simulated using the govern equations obtained from the Newton's second law. Then, time series of the system's average magnetization are calculated for an alternating external magnetic field. Since the system is random, due to the probabilistic nature of Brownian motion, 50 simulations are performed and a mean value of all samples are obtained. With this, a parametric analysis is carried out, in order to identify the parameters that most affect the dynamical behavior of the system. In this manner, the effect of the hysteresis curve, the phase space and the Poincaré map are analyzed in every case, with the average magnetization being the state variable. After this, in the perpendicular direction of the external magnetic field, a Couette alternating flow is applied and the dynamical analysis is carried out. So, a comparison between the system with Coeutte flow and the one without this shear mechanism is performed. Therefore, the main target of this work is to find the best conditions for the magnetic hyperthermia, by means of analyzing the system's internal energy production. Thus, simulation results show that a higher frequency of the oscillating magnetic field is desirable and that shear flow is not recommended for the cancer treatment.*
Keywords: *magnetic hyperthermia, magnetic heating, ferrofluid, magnetic fluid, nonlinear dynamics*

1. INTRODUCTION

Magnetic Hyperthermia (MH) is a medical procedure that aims the destruction of cancer cells by means of applying a magnetic field and a ferrofluid in the area of the tumor (Liu *et al.*, 2020). The magnetic fluid moves due to the applied field and its motion generates internal energy within the system (Rosensweig, 2002). Thus, with the temperature slightly increased from the normal human body-temperature of 37ºC, the cancer cells die, whereas the healthy tissue remains alive.

Hyperthermia methods that increase the cancerous cells temperature, used to to decelerate or stop the growth of the tumor, are known since the 19th century (Uhlmann *et al.*, 2002). However, the downside of most of these treatments, such as focused radio-frequency, ultrasound irradiation and local thermal contact, are the side effects produced in the healthy tissue by the high temperature (Odenbach, 2009). Because of that, MH has the advantage of being a local therapy with fewer side effects in comparison with chemotherapy and radiotherapy (Thiesen and Jordan, 2008). Furthermore, according to the authors, MH can be used in combination with other treatments, increasing their efficacy. The MH treatment has an edge, considering that is effective and minimally invasive and can destroy the cancer or detain its expansion (Silva *et al.*, 2010).

To apply the MH in patients, one must use a Ferrofluid (FF), that is, a conglomerate of Magnetic Nanoparticles (MNPs) dispersed in a liquid carrier (Gontijo and Cunha, 2015). With the development of nanotechnology, FFs were created by Stephen (1965) at NASA and improved significantly the MH method (Liu *et al.*, 2020). Moreover, FFs are considered smart nanomaterials (Huang *et al.*, 2017), (Coisson *et al.*, 2017).

In the constitution of a MNP, a surfactant covers the magnetic core surface in order to avoid the agglomeration of particles due to the magnetic attractive forces (Huang *et al.*, 2017). To exemplify this, Fig. 1 shows the structure of a MNP, with its core made with magnetic material (in violet) and the surfactant shell (in blue).

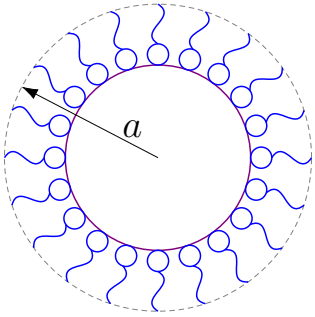

Figura 1: **Representation of a magnetic particle. Magnetic core (in violet) and surfactant layer (in blue), where a is the particle's radius. Figure adapted from Arias *et al.* (2018).**

Regarding the literature about MH, one can note that the dynamical point-of-view of the problem has not been yet considered. Thus, the contribution of this work consists in the dynamical characterization of the nonlinear system, and the analysis of the relationship between dynamical behavior and increase of temperature. In order to simulate a FF, a system of magnetic particles governed by nonlinear differential equations is studied.

In this manner, the main target of the study is to determine the the best-case scenario for MH. Therefore, the specific targets are: simulate the system with only magnetic field, simulate the system with magnetic field and shear flow, evaluate the internal energy per unit volume for both cases and different parameters and select the case with the highest internal energy.

2. MATHEMATICAL MODELING

The system studied in this work is the same one analyzed by Gontijo and Cunha (2015) with a few modifications. All variables treated in this work are nondimensional. The statistical convergence of the system has been analyzed by Gontijo and Cunha (2015) and Gontijo and Cunha (2017).

Fig. 2 displays the frontal view of the tridimensional system of MNPs, which are represented by black spheres of same radius. The limit of the domain is represented by dashed gray lines and the unit vectors of the Cartesian coordinate system by $\hat{\mathbf{x}}$, $\hat{\mathbf{y}}$ and $\hat{\mathbf{z}}$. Let $i \in \mathbb{N}$ be the index of the i-th particle in the system, such that $1 \leq i \leq N$, where N is the total number of particles. Thus, the i-th particle contains a magnetic moment dipole vector with its own orientation ($\mathbf{m}_i$). Initially, at Fig, 2a, the MNPs are randomly distributed and the sum of all dipole contributions equals to zero. On the other hand, at Fig. 2b, when a dimensionless external magnetic field ($\mathbf{H}$) is applied, the MNPs show a favorable direction and a magnetization is observed ($\mathbf{M}$).

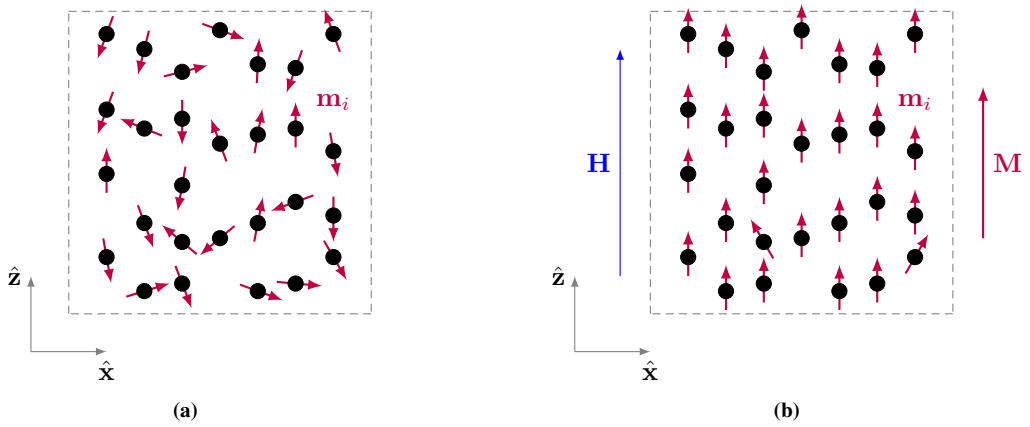

Figura 2: **System of MNPs dispersed in a liquid carrier: Each particle has a magnetic moment dipole vector ($\mathbf{m}_i$), domain limits represented by gray dashed lines and origin represented by gray vectors. (a) Configuration of particles randomly distributed. (b) Particles under the influence of the external magnetic field ($\mathbf{H}$). As a consequence, the particles show a preferential direction and a magnetization ($\mathbf{M}$).**

In this work, it is considered $N = 300$ particles for all simulations. Thus, the magnetization of the system for a given time is described by Eq. (1),

$$\mathbf{M}(t) = \frac{1}{V}\sum_{i=1}^{300} \mathbf{m}_i(t), \tag{1}$$

where: t is the dimensionless time, $\mathbf{M}(t)$ is the dimensionless magnetization which depends upon the time, V is the dimensionless volume of the system, i is the index of each particle and $\mathbf{m}_i(t)$ is the dimensionless magnetic dipole moment vector of the i-th particle.

In order to monitor the time evolution of the system, the governing equations for the motion of each particle is studied by the Newton's second law and then solved using the fourth order Runge-Kutta numerical method. As a consequence, the translational motion of the i-th particle in the nondimensional form is described by Eq. (2),

$$\mathrm{St}\frac{\mathrm{d}\mathbf{u}_i}{\mathrm{d}t} = -\mathbf{u}_i + \mathbf{g} + \mathbf{F}_{\mathbf{m}i} + \mathbf{F}_{\mathbf{B}i} + \mathbf{F}_{\mathbf{r}i} + \mathbf{F}_{\mathbf{c}i}, \tag{2}$$

in which: St is the Stokes number, $\mathbf{u}_i$ is the nondimensional velocity vector field for the i-th particle, $\mathbf{g} = -\hat{\mathbf{z}}$ is the dimensionless gravitational field and $\mathbf{F}_{\mathbf{m}i}$, $\mathbf{F}_{\mathbf{B}i}$, $\mathbf{F}_{\mathbf{r}i}$ and $\mathbf{F}_{\mathbf{c}i}$ are, respectively, the nondimensional magnetic, brownian, repulsive and contact forces under the i-th particle.

The repulsive and contact dimensionless forces, $\mathbf{F}_{\mathbf{r}i}$ and $\mathbf{F}_{\mathbf{c}i}$, are calibrated to avoid particle overlap in the simulations (Gontijo and Cunha, 2015). As stated by the author, the dimensionless magnetic force is given by Eq. (3),

$$\mathbf{F}_{\mathbf{m}i} = \left\{ \sum_{\substack{j=1 \\ j\neq i}}^{300} \frac{24\lambda}{\mathrm{Pe}\, r_{ij}^4} \Big[\left(\mathbf{m}_i \cdot \mathbf{m}_j\right) \hat{\mathbf{r}}_{ij} + \left(\mathbf{m}_i \cdot \hat{\mathbf{r}}_{ij}\right) \mathbf{m}_j + \left(\mathbf{m}_j \cdot \hat{\mathbf{r}}_{ij}\right) \mathbf{m}_i + \right.$$
$$\left. - 5 \left(\mathbf{m}_i \cdot \hat{\mathbf{r}}_{ij}\right) \left(\mathbf{m}_j \cdot \hat{\mathbf{r}}_{ij}\right) \hat{\mathbf{r}}_{ij} \Big] \right\} + \frac{\alpha}{\mathrm{Pe}} \left(\mathbf{m}_i \cdot \nabla \mathbf{H}\right), \tag{3}$$

where: α is the Langevin parameter that measures the relation between magnetic energy and thermal energy, Pe is the Peclet number that correlates the times scales of brownian diffusion and convection flow, λ is the dipole-dipole interaction parameter, defined as magnetic forces from dipole-dipole effects divided by the brownian force (Gontijo and Cunha, 2017), r_{ij} is the distance between the center of mass from the i-th and j-th particle, $\hat{\mathbf{r}}_{ij}$ is the unitary vector that points to the j-th particle from the i-th particle and $\mathbf{H}$ is the non-dimensional external magnetic field vector.

The brownian random force is given by Eq. (4),

$$\mathbf{F}_{\mathbf{B}i} = \left(\frac{6}{\mathrm{Pe}\delta\tau}\right)^{1/2} \boldsymbol{\xi}. \tag{4}$$

in which: $\boldsymbol{\xi}$ is a randomic vector with Gaussian distribution between the values -1 and 1 and $\delta\tau$ is a dimensionless typical time scale from the brownian motion.

For the rotational motion of the i-th particle, Newton's second law yields Eq. (5),

$$\mathrm{St}_r \frac{\mathrm{d}\boldsymbol{\omega}_i}{\mathrm{d}t} = -\boldsymbol{\omega}_i + \mathbf{T}_{\mathbf{m}i} + \mathbf{T}_{\mathbf{B}i}, \tag{5}$$

where: St_r is the rotational Stokes number, $\boldsymbol{\omega}_i$ is the dimensionless angular velocity vector for the i-th particle, $\mathbf{T}_{\mathbf{m}i}$ and $\mathbf{T}_{\mathbf{B}i}$ are, respectively, is the dimensionless magnetic and brownian torque under the i-th particle.

The magnetic torque is given by Eq. (6),

$$\mathbf{T}_{\mathbf{m}i} = \left\{ \sum_{\substack{j=1 \\ j\neq i}}^{300} \frac{24\lambda}{\mathrm{Pe}_r r_{ij}^3} \Big[-\frac{1}{3} \left(\mathbf{m}_i \times \mathbf{m}_j\right) + \left(\mathbf{m}_j \cdot \hat{\mathbf{r}}_{ij}\right) \left(\mathbf{m}_i \times \hat{\mathbf{r}}_{ij}\right) \Big] \right\} + \frac{\alpha}{\mathrm{Pe}_r} \left(\mathbf{m}_i \times \mathbf{H}\right), \tag{6}$$

in which: $\mathrm{Pe}_r = (3/4)\,\mathrm{Pe}$ is the rotational Peclet number.

And the brownian torque is given by Eq. (7)

$$\mathbf{T}_{\mathbf{B}i} = \left(\frac{6}{\mathrm{Pe}\delta\tau}\right)^{1/2} \boldsymbol{\xi}. \tag{7}$$

The nondimensionalization applied for the system is shown at Eq. (8),

$$\mathbf{u}_i = \frac{\mathbf{u}_{d_i}}{U_s}, \quad \boldsymbol{\omega}_i = \frac{\boldsymbol{\omega}_{d_i} a}{U_s} \quad \text{and} \quad t = \frac{t_d U_s}{a}, \tag{8}$$

where: $\mathbf{u}_{d_i}$ and $\boldsymbol{\omega}_{d_i}$ are, respectively, the dimensional velocity and dimensional angular velocity vectors for the i-th particle, t_d is the dimensional time, a is the particle's radius and U_s is the particle's terminal velocity from Stokes' law.

For all simulations perfomed in this work, it was adopted the values $\mathrm{St} = 0.1$ and $\mathrm{St}_r = 0.01$, due to the calibration of repulsive and contact forces (Gontijo, 2013).

In respect of boundary conditions, the system has periodic conditions at the limits of each direction, such that, if a particle crosses the right side of the domain, it is dislocated to the left side and vice-versa. Regarding the initial condition, a random distribution configuration of particles is applied in each simulation.

Since the system is random, by virtue of brownian motion, each simulation gives a different behavior of the magnetization, $\mathbf{M}(t)$. To converge this information into a single data, 50 different and independent simulations are performed and a mean value of all samples are obtained, descrided by Eq. (9),

$$\overline{\mathbf{M}}(t) = \frac{1}{50}\sum_{k=1}^{50}\mathbf{M}_k(t) \tag{9}$$

in which: $\overline{\mathbf{M}}(t)$ is the average magnetization, $k \in \mathbb{N}$ is the index of each realization and $\mathbf{M}_k(t)$ is the magnetization obtained for the k-th realization.

The average magnetization is the state variable treated in this work to analyze the system. With it, the time response ($\overline{\mathbf{M}}$ vs t), the phase space ($\dot{\overline{\mathbf{M}}}$ vs $\overline{\mathbf{M}}$) and the hysteresis curve ($\overline{\mathbf{M}}$ vs $\mathbf{H}$) are analyzed. For this manner, the variable is described in the cartesian coordinate system,

$$\overline{\mathbf{M}} = \overline{M}_x\hat{\mathbf{x}} + \overline{M}_y\hat{\mathbf{y}} + \overline{M}_z\hat{\mathbf{z}}, \tag{10}$$

where: $\overline{M}_x$, $\overline{M}_y$ and $\overline{M}_z$ are, respectively, the x, y and z components of the average magnetization. For the determination $\dot{\overline{\mathbf{M}}}$, finite difference method was applied.

Together with the phase space, the Poincaré map can be represented, that is, a qualitative method to characterize the dynamical system (Savi, 2006). To do such, one must chose a cutting plane in the phase space. Considering the external magnetic field as a periodic function, the Poincaré section can be defined as the state of the system when $t = nT$, where $n \in \mathbb{N} \mid n = \{1, 2, 3\ \ldots\}$ is a natural number and T is the period of $\mathbf{H}$. In other words, every time the external magnetic field completes a cycle, a single dot is marked in the phase space. However, since the solution of Eqs. (2) and (5) given by Runge-Kutta method is discrete, the Poincaré map may be localized between 2 numerical values. In order to solve this and to obtain a more precise representation of the Poincaré map, interpolation was applied to the variables $\dot{\overline{\mathbf{M}}}(t)$ and $\overline{\mathbf{M}}(t)$ for the value $t = nT$.

Under the hypothesis that the external magnetic field is harmonic, for a given cycle of the magnetic field, the increment of internal energy per unit volume (Rosensweig, 2002) can be calculated with Eq. (11),

$$\Delta U = -\oint \overline{\mathbf{M}}(t)\cdot \mathrm{d}\mathbf{H}(t), \tag{11}$$

in which: $\mathbf{H}$ is the nondimensional harmonic magnetic field and ΔU is the dimensionless change of internal energy for 1 cycle of $\mathbf{H}$ from all 50 realizations of the system. In other words, the internal energy is calculated through the area of the curve delimited by $\overline{\mathbf{M}}$ and $\mathbf{H}$ (hysteresis curve).

With the assumption that the external magnetic field is applied only in the $\hat{\mathbf{z}}$ direction, Eq. (11) yields Eq. (12),

$$\Delta U = -\oint \overline{M}_z\,\mathrm{d}H_z, \tag{12}$$

where: H_z is the z component of the dimensionless magnetic field.

Since the system regarded in this work is nonlinear, the contribution of ΔU can change for each cycle. Because of this, ΔU is determined by the mean area, that is, the sum of the areas obtained for all cycles divided by the number of cycles. Therefore, Eq. (12) becomes Eq. (13)

$$\Delta U = -\frac{1}{N_{cyc}}\int \overline{M}_z\,\mathrm{d}H_z, \tag{13}$$

in which: N_{cyc} is the total number of cycles presented by the external magnetic field. In this work, it was considered $N_{cyc} = 20$.

3. RESULTS

The results are divided into 2 parts: one with the system being subjected only to an harmonical Langevin parameter in the $\hat{\mathbf{z}}$ direction and one with the Langevin parameter in the $\hat{\mathbf{z}}$ direction and with a shear rate mechanism in the $\hat{\mathbf{y}}$ direction at the same time.

3.1 External Magnetic Field

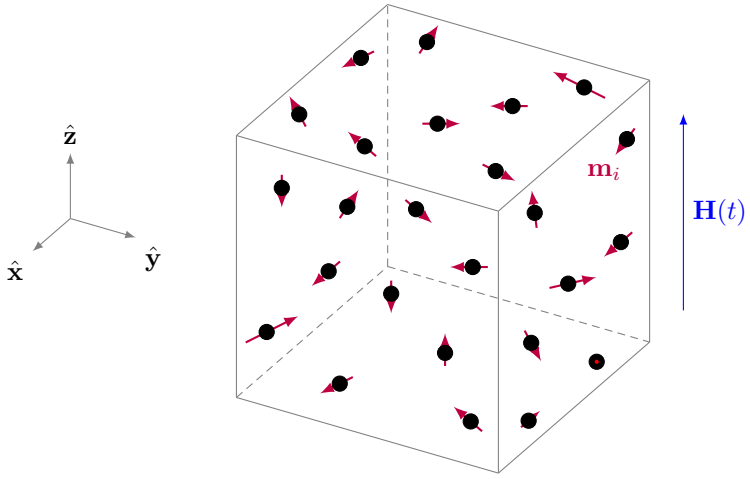

Figura 3: **Representation of the system under only a dimensionless magnetic field. An external magnetic field with harmonic behavior is applied in the $\hat{\mathbf{z}}$ direction ($\mathbf{H}$). Particles are represented by black dots and their dipole vector in red ($\mathbf{m}_i$).**

Figure 3 shows the system treated in this section. Note that the only excitation is the external magnetic field in the $\hat{\mathbf{z}}$ direction. In this way, only the z component of the average magnetization is significant, whereas the x and y components present values close to zero.

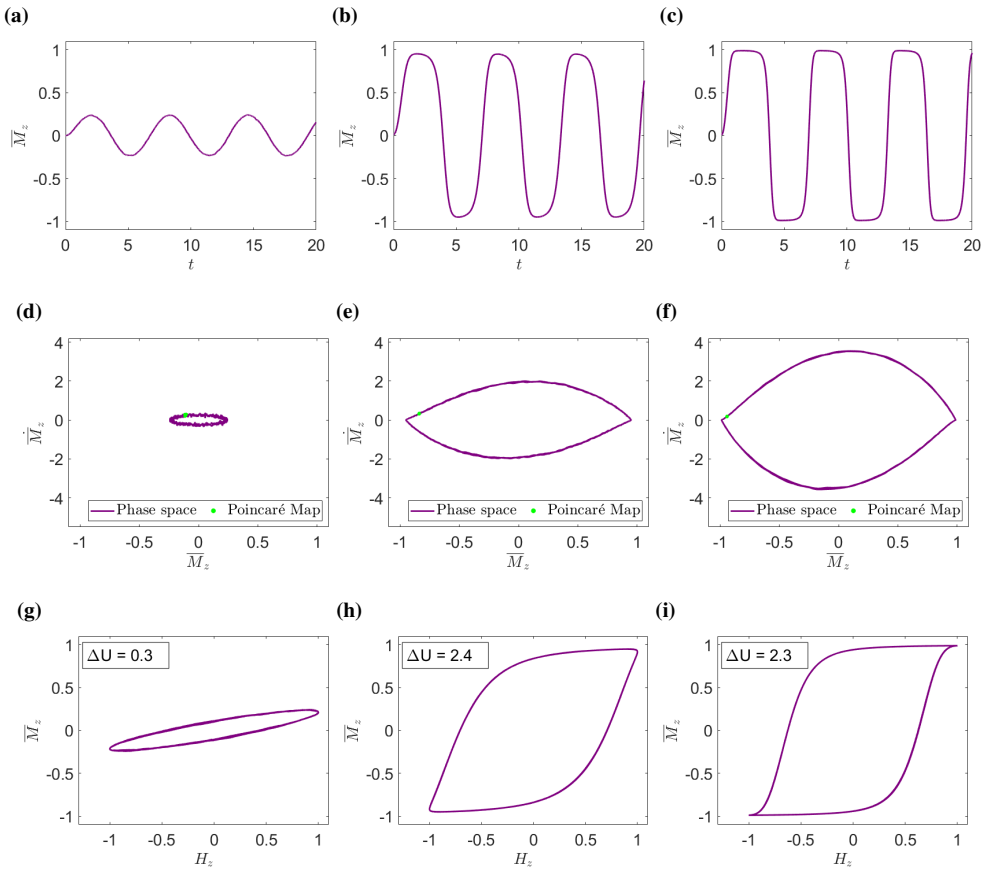

Figura 4: **Scan of the variable** Pe **for the constant values of** $\alpha = 1$, $\omega_h = 1$, $\lambda = 1$, $\phi = 1\%$. **(a), (b) and (c) Magnetization's z component time response. (d), (e) and (f) Phase space (in violet) and Poincaré map (in green). (g), (h) and (i) Hysteresis curve. (a), (d) and (g)** $\mathrm{Pe} = 1$**. (b), (e) and (h)** $\mathrm{Pe} = 5$**. (c), (f) and (i)** $\mathrm{Pe} = 10$**.**

The time evolution of the external magnetic field is given by Eq. (14),

$$\mathbf{H}(t) = \alpha \sin(\omega_h t)\hat{\mathbf{z}}, \tag{14}$$

in which: ω_h is the dimensionless angular frequency associated with the dimensionless magnetic field.

From Eq. (14), the period of $\mathbf{H}$ is $T = 2\pi/\omega_h$. As a consequence, the Poincaré map of the system is determined by the stroboscopically aquired points by $t = 2\pi n/\omega_h$, where $n \in \mathbb{N} \mid n = \{1, 2, 3 \ \dots\}$ is a natural number.

A parameter scan is performed for multiple variables of the system. Figure 4 shows the results scanning the variable Pe, the Peclet number, with the constants values of $\alpha = 1$, $\omega_h = 1$, $\lambda = 1$ and $\phi = 1\%$ (low concentration). More specfically, the first column of Fig. 4 displays the results for $\mathrm{Pe} = 1$, the second column presents the results for $\mathrm{Pe} = 5$, and so forth. In a similar way, the first line of Fig. 4 shows the time response of the average magnetization 's z component for all values of Pe, the second line presents the phase space (in violet) with the Poincaré map (in green) and the third line displays the hysteresis curve. Lastly, regarding the hysteresis curve and the phase space, the results are shown in the steady-state condition for all cases in this work.

At Figs. 4a, 4d and 4g, one can see the behavior of the system for a low Peclet number ($\mathrm{Pe} = 1$). In this case, the brownian random motion has a significant influence in the system, which produces a noisy signal of the phase space at Fig. 4d. Moreover, the time response at Fig. 4a is periodic with period 1, as displayed by the Poincaré map at Fig. 4d. For this case, the area under the curve at Fig. 4g provides a internal energy change of $\Delta U = 0.3$.

At Figs. 4b, 4e and 4h, the system is shown for an intermediate value of the Peclet number ($\mathrm{Pe} = 5$). In comparison with the prior case, the time response of Fig. 4b has increase its amplitude. As a consequence, the area provided by Fig. 4h has increased as well and reached a value of $\Delta U = 2.4$, a better case for the MH treatment. Furthermore, the phase space at Fig. 4e has lost the noisy feature displayed by the previous case. Therefore, the brownian motion has a low influence under the system behavior. Lastly, the result continues to be periodic of period 1, as shown by the single dot Poincaré map at Fig. 4e.

At Figs. 4c, 4f and 4i, the system is shown for a high value of the Peclet number ($\mathrm{Pe} = 10$). In this case, the time response at Fig. 4c approximates to a square wave. This happens because the system has reached the saturation magnetization. Consequently, the amplitude of the signal is bounded by the limit values 1 and -1. Hence, the hysteresis curve at Fig. 4i presents 2 sharps edges and the area of the curve has slightly decrease from the prior simulation, resulting in $\Delta U = 2.3$. Even so the time response is similar to a square wave, the signal remains periodic, as stated by the period 1 behavior of the Poincaré map at Fig. 4f.

Comparing Figs. 4g, 4h and 4i, one can note the highest internal energy per unit volume is $\Delta U = 2.4$. Thus, the value $\mathrm{Pe} = 5$ is set as the best-case scenario for the next simulations.

Figure 5 displays the results obtained for the scan of the variable α with the constants values of $\mathrm{Pe} = 5$ (decided by the previous scan), $\omega_h = 1$, $\lambda = 1$ and $\phi = 1\%$. For this scan, the values $\alpha = 1$, $\alpha = 1$ and $\alpha = 10$ were considered.

Figures 5a, 5d and 5g shows the same results obtained at Figs. 4b, 4e and 4h, but in a different scale for the sake of comparison. At Fig. 5b and 5c, one can notice that as α increases, the closer the time response is to a square wave. This is due to the fact that, with a higher α, the external magnetic field is more intense. Consequently, the magnetization reaches the saturation value faster than a simulation with low α. After reaching this condition, as the external magnetic field increases its values even more, the magnetization is bounded by the value of 1, sharpening the edges of the square wave. Because of this, the sharps points of the hysteresis curve suffer stretching, as displayed by Fig. 5h and 5i. Furthermore, one can realize that not only the sharp edges have stretched, but the curve has extended as well. Thus, the area under the hysteresis curve is higher for the case with high α, with a peak value of $\Delta U = 11.6$. Regarding the phase space, one can see that the response remains a periodic with period 1 at Fig. 5e and 5f.

Finally, by the comparision of Figs. 4h, 5h and 5i, the value $\alpha = 10$ is chosen for the nex simulations, on account of it yields the highest internal energy per volume for the α scan.

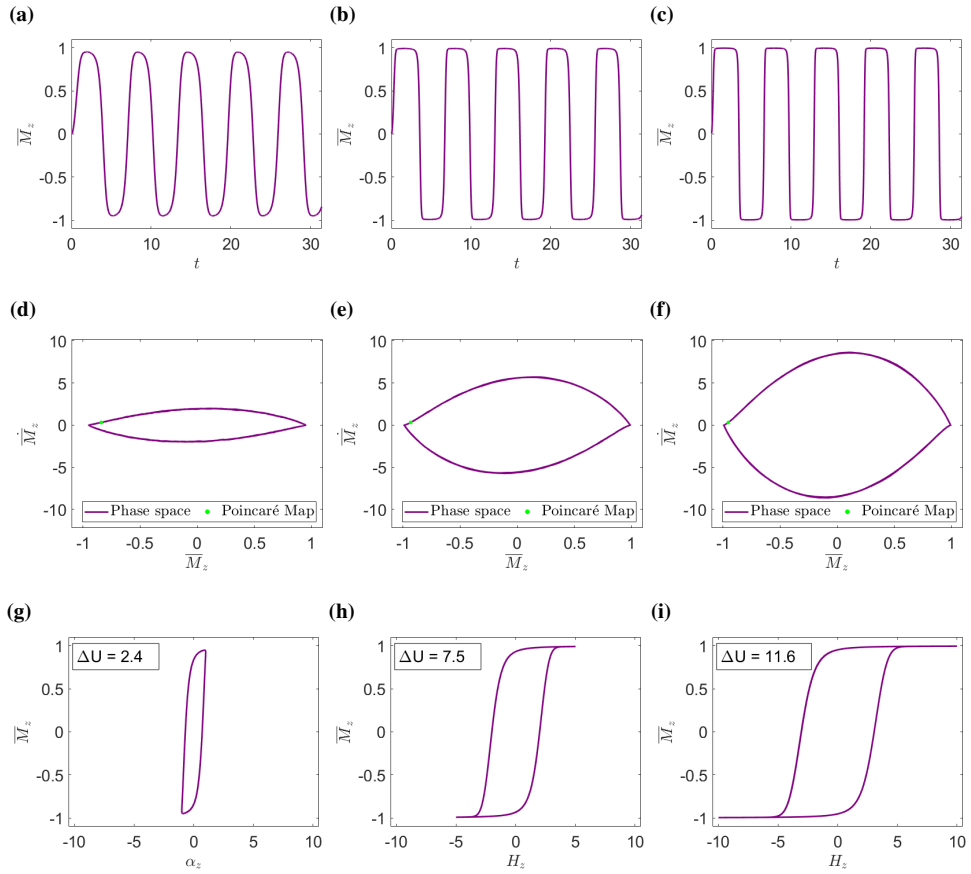

Figura 5: **Scan of the variable α for the constant values of $\mathrm{Pe} = 5$, $\omega_h = 1$, $\lambda = 1$, $\phi = 1\%$. (a) and (b) Magnetization's z component time response. (c) and (d) Phase space (in violet) and Poincaré map (in green). (e) and (f) Hysteresis curve. (a), (c) and (e) $\alpha = 5$. (b), (d) and (f) $\alpha = 10$.**

Figure 6 displays the results scanning the variable ω_h, with the constants values of $\mathrm{Pe} = 5$, $\omega_h = 10$, $\lambda = 1$ and $\phi = 1\%$. For this scan, it was considered the values $\omega_h = 5$ and $\omega_h = 10$. With the purpose of compare the system's changes for this scan, Figures 6a, 6d and 6g displays the same graphs obtained at Figs. 5c, 5f and 5i in a different scale.

At Fig. 6b, one can see the time response is smoother than Fig. 5c. Similarly, the sharps edges of the hysteresis curve at Fig. 6h are smaller compared to Fig. 5i. This occurs because of the high frequency of the external magnetic field, that is, as the harmonic magnetic field changes faster than before, the magnetization spends less time in the saturation bounded limit. As a result, since there is a lag between $\mathbf{M}$ and $\mathbf{H}$, the edges of the time response become less prominent. However, the area under the curve has increased and reached a value of $\Delta U = 28.8$.

At Fig. 6c, one can notice that the magnetization has a higher frequency, as expected, and the effect of smaller edges is more intense than before. More specifically, at Fig. 6i, one can see that the sharps edges of the hysteresis curve have disappeared. This means that, despite the system being closer to the saturation limit, it has not reached the bounded limit completely. As a result, the area at Fig. 6i is even higher than the one in the the previous simulation, achieving $\Delta U = 36.2$. This indicates that the sharps edges at the hysteresis curve are not an advantage for the production of internal energy. About the Poincaré map, in both cases displayed at Figs. 6e and 6f, the results remain periodic in period 1.

Based on the analysis of Fig. 6, the value $\omega = 10$ is chosen for the next simulations due to the highest change of internal energy, which is highlighted at Fig. 6i.

Regarding the last variables, the scan of the dipole-dipole interaction parameter (λ) for the values $\lambda = 1$, $\lambda = 5$ and $\lambda = 10$ has not shown significant changes in the system's behavior. Because of this, the value $\lambda = 1$ was adopted. In a similar way, the results for a high concentration of particles ($\phi = 15\%$) are similar to the ones obtained for a low concentration ($\phi = 1\%$). Thus, the results will focus on the cases with volume fraction equal to $\phi = 1\%$.

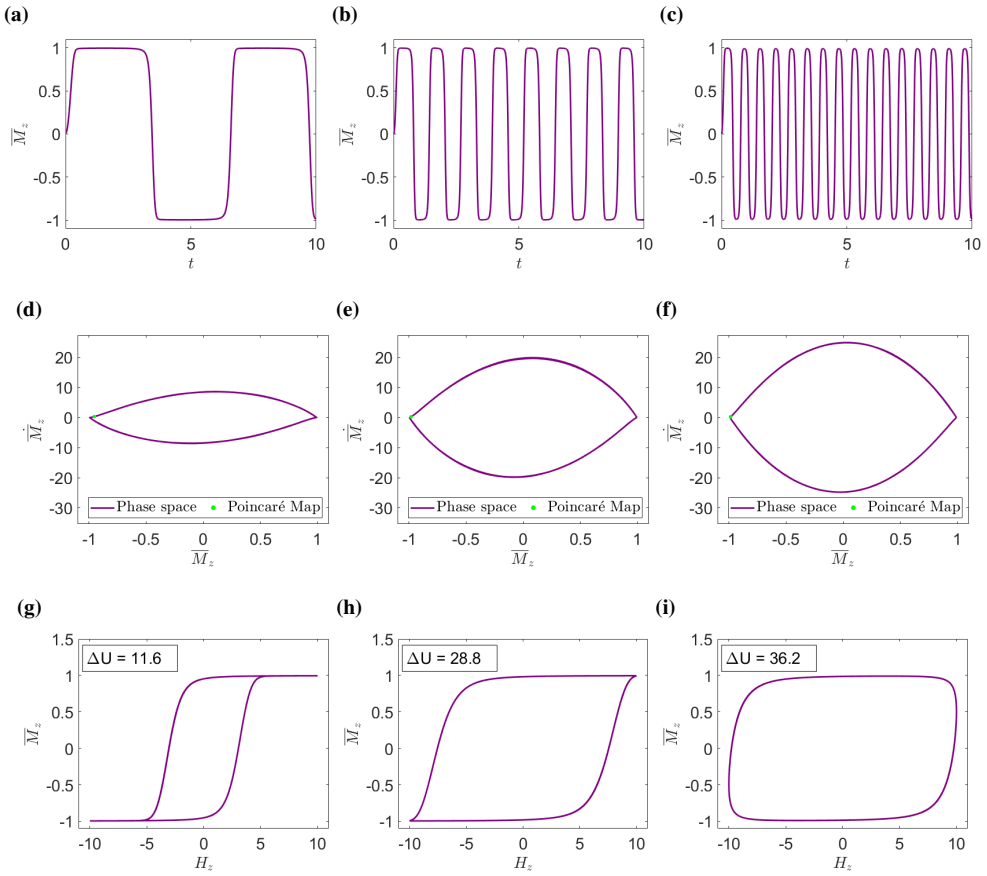

Figura 6: **Scan of the variable ω_h for the constant values of $\mathrm{Pe} = 5$, $\alpha = 10$, $\lambda = 1$, $\phi = 1\%$. (a) and (b) Magnetization's z component time response. (c) and (d) Phase space (in violet) and Poincaré map (in green). (e) and (f) Hysteresis curve. (a), (c) and (e) $\omega_h = 5$. (b), (d) and (f) $\omega_h = 10$.**

3.2 External Magnetic Field and Shear Rate

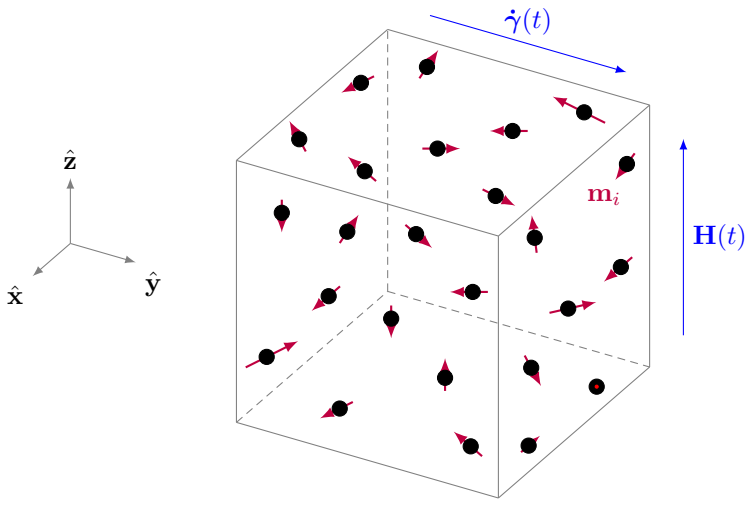

Figura 7: **Representation of the system under both dimensionless magnetic field and shear rate. In addition to the external magnetic field in the $\hat{\mathbf{z}}$ direction ($\mathbf{H}$), a dimensionless shear rate motion with harmonic behavior is applied in the $\hat{\mathbf{y}}$ direction ($\dot{\boldsymbol{\gamma}}$). Particles are represented by black dots and their dipole vector in red ($\mathbf{m}_i$).**

In this section, a new excitation is added to the system, which is displayed by Fig. 7. There are two excitations at the same time: a nondimensional harmonic external magnetic field at the $\hat{\mathbf{z}}$ direction ($\mathbf{H}(t)$) and a nondimensional harmonic shear rate motion at the $\hat{\mathbf{y}}$ direction ($\dot{\boldsymbol{\gamma}}(t)$). As a consequence, both the z and y components of the average magnetization are significant, while the x components of $\overline{\mathbf{M}}$ is always close to zero. Under this shear rate motion combined with

magnetic field, the production of internal energy is analyzed and compared with the case where only the magnetic field is present.

The time evolution of the shear rate is given by Eq. (15),

$$\dot{\boldsymbol{\gamma}}(t) = \dot{\gamma}_0 \sin(\omega_s t)\hat{\mathbf{y}}, \tag{15}$$

where: $\dot{\boldsymbol{\gamma}}$ is the shear rate vector field, $\dot{\gamma}_0$ is the dimensionless shear rate amplitude and ω_s its dimensionless angular frequency. Eq. (15) follows Newton's viscosity law, in a way that it describes an alternating Couette flow applied to the system. More specifically, the intensity of the shear motion is linearly distributed in the $\hat{\mathbf{z}}$ direction.

Figure 8 shows the results scanning the variable $\dot{\gamma}_0$, the amplitude of the shear rate, with the constants values of $\alpha = 10,\ \mathrm{Pe} = 5, \omega_h = 10, \omega_s = 1, \lambda = 1$ and $\phi = 1\%$. Since the $\hat{\mathbf{y}}$ component of magnetization is now significant, the graphs have been rearranged: the first column of Fig. 8 displays the results for $\dot{\gamma}_0 = 1$, the second column shows graphs for $\dot{\gamma}_0 = 5$ and the third column for $\dot{\gamma}_0 = 10$. The first, second and third line of Fig. 8 displays, respectively, the time series, the phase space and the hysteresis curve for the $\hat{\mathbf{z}}$ direction (in violet). Similarly, the fourth and fifth line of Fig. 8 shows, respectively, the time series and the phase space for the $\hat{\mathbf{y}}$ direction (in black). Since there is no external magnetic field applied in the $\hat{\mathbf{y}}$ direction, such that $H_y = 0$, the hysteresis curve of the $\hat{\mathbf{y}}$ is a single vertical line with zero area. So, the internal energy contribution of the $\hat{\mathbf{y}}$ direction is equal to zero. Thus, the internal energy is calculated by the same way as before, by the area of only $\overline{M}_z$ and H_z.

Figure 8a shows the time series in the $\hat{\mathbf{z}}$ direction for $\dot{\gamma}_0 = 1$, which resembles a periodic behavior. Moreover, the phase space of the $\hat{\mathbf{z}}$ direction at Fig. 8d displays 3 different orbits and its Poincaré map reveals 1 dense point, meaning a response periodic with period 1. In a similar way, the hysteresis curve has 3 different shapes, all of them obtained in steady-state regime, meaning that the graph continuously changes from those 3 different configurations. Still in the hysteresis curve, the production of internal energy has significantly decreased: an amount of $\Delta U = 31.6$ was achieved, while in the case without shear motion a value of $\Delta U = 36.2$ was obtained at Fig. 6i, meaning that the addition of shear motion is not beneficial to the MH treatment. In the $\hat{\mathbf{y}}$ direction, Fig. 8j indicates an interesting pattern for the time series, while the Poincaré map at Fig. 8m points a periodic response with period 5.

Figure 8b displays the time response in the $\hat{\mathbf{z}}$ direction for $\dot{\gamma}_0 = 5$, a more intense shear rate. In this case, one can notice an interesting periodic pattern, full of sharp edges, created by the interactions of the system's $\hat{\mathbf{y}}$ and $\hat{\mathbf{z}}$ components. This behavior is illustrated by the phase space and Poincaré map in the $\hat{\mathbf{z}}$ direction at Fig. 8e by a periodic response with period 5. As a consequence, the hysteresis curve at Fig. 8h shows several intersections points with itself. Such pattern give rise for negative areas in the calculation of internal energy, stemming from the demagnetization work. As a consequence, the production of internal energy is low, such that $\Delta U = 8.6$. In the $\hat{\mathbf{y}}$ direction, Fig. 8k shows the same change observed in the $\hat{\mathbf{z}}$ direction and the Poincaré map at Fig. 8n indicates a periodic response with period 8, that is, a different period from the $\hat{\mathbf{z}}$ direction.

Lastly, Figure 8c shows the time series in the $\hat{\mathbf{z}}$ direction for the value $\dot{\gamma}_0 = 10$. For this case, the nonlinear behavior of the system is amplified. The Poincaré map in the $\hat{\mathbf{z}}$ direction at Fig. 8f indicates a periodic orbit with period 5, the same period as Fig. 8e. Unfortunately, the nonlinear behavior has drastically decreased the internal energy production, as shown by Fig. 8i and the value $\Delta U = 0.5$. Regarding the $\hat{\mathbf{y}}$ direction, the time series at Fig. 8l displays a similar behavior from Fig. 8c and the Poincaré map at Fig. 8o shows a periodic orbit with period 10, a higher period than the previous case at Fig. 8n.

With this analysis, $\dot{\gamma}_0 = 1$ is chosen as the best value for shear motion ($\Delta U = 31.6$ at Fig. 8g), even though the case without the shear mechanism produces a better scenario for internal energy production ($\Delta U = 36.2$ at Fig. 6i).

Considering the variable ω_s, the scan of the shear rate frequency for the values $\omega_s = 1$, $\omega_s = 5$ and $\omega_s = 10$ has not shown significant changes in the system's behavior. As a contrast to the frequency of the external magnetic field (ω_h), which increases greatly the change in internal energy, the frequency of the shear rate motion have an negative effect in the production of internal energy, being unrecommended for MH.

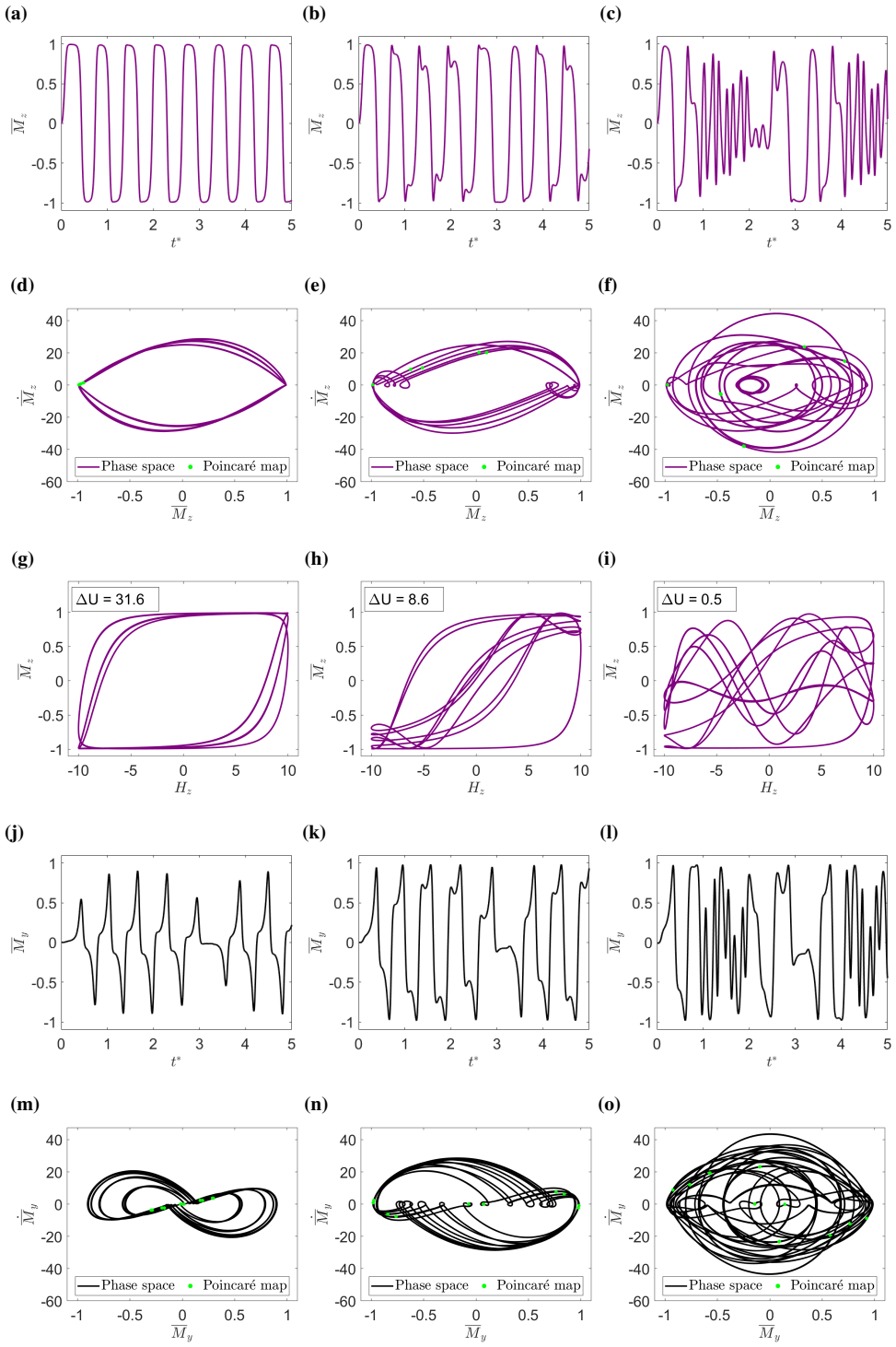

Figura 8: **Scan of the variable $\dot{\gamma}_0$ for the constant values of** $\mathrm{Pe} = 5$, $\alpha = 10$, $\omega_h = 10$, $\omega_s = 1$, $\lambda = 1$, $\phi = 1\%$. **(a), (b) and (c) Magnetization's time response for the $\hat{z}$ direction (in violet). (d), (e) and (f) Phase space for the $\hat{z}$ direction (in violet) and corresponding Poincaré map (in green). (g), (h) and (i) Hysteresis curve. (j), (k) and (l) Magnetization's time response for the $\hat{y}$ direction (in black). (m), (n) and (o) Phase space for the $\hat{y}$ direction (in black) and corresponding Poincaré map (in green). (a), (d), (g), (j) and (m) $\dot{\gamma}_0 = 1$. (b), (e), (h), (k) and (n) $\dot{\gamma}_0 = 5$. (c), (f), (i), (l) and (o) $\dot{\gamma}_0 = 10$.**

4. CONCLUSION

In the performed simulations, for the case where only the magnetic field is present, it was shown that the highest value of α and ω_h (frequency of the oscillating magnetic field) is desirable, since it yields the highest amount of internal energy for the method of MH. Regarding the Peclet number, an intermediate value of the variable has produced the highest internal energy ($\mathrm{Pe} = 5$), whereas the variables λ and the concentration of particles have not change the system's behavior in a significant way. Furthermore, for the ω_h scan, it was shown that sharps edges at the hysteresis curve decreases the

value of ΔU, such that it is not beneficial. When a shear rate motion was introduced in the system, the internal energy decreased for all cases in comparison with the simulation without shear. In this case, a more complex time response and phase space were obtained, related to periodic response with higher periodicity. Despite the magnetic field frequency being an important parameter to elevate the internal energy of the system, the shear rate frequency has an negative effect in the same variable. Considering that the activation of the shear rate mechanism requires an energy consumption and it does not increase the internal energy production, the shear motion is not recommended for the treatment of MH.

5. ACKNOWLEDGMENTS

The authors would like to acknowledge the support of Coordenação de Aperfeiçoamento de Pessoal de Nível Superior (CAPES), the support of Fundação de Apoio à Pesquisa e Inovação do Distrito Federal (FAPDF) and the helpful insights of the professor Taygoara Felamingo de Oliveira for this work.

6. REFERENCES

Arias, L.S., Pessan, J.P., Vieira, A.P.M., Lima, T.M.T.d., Delbem, A.C.B. and Monteiro, D.R., 2018. "Iron oxide nanoparticles for biomedical applications: a perspective on synthesis, drugs, antimicrobial activity, and toxicity". *Antibiotics*, Vol. 7, No. 2, p. 46.

Coisson, M., Barrera, G., Celegato, F., Martino, L., Kane, S.N., Raghuvanshi, S., Vinai, F. and Tiberto, P., 2017. "Hysteresis losses and specific absorption rate measurements in magnetic nanoparticles for hyperthermia applications". *Biochimica et Biophysica Acta (BBA)-General Subjects*, Vol. 1861, No. 6, pp. 1545–1558.

Gontijo, R.G., 2013. *Micromecânica e microhidrodinâmica de suspensões magnéticas*. Doutorado, Departamento de Engenharia Mecânica, Universidade de Brasília, Brasília, DF. Publicação ENM.TD - 19A, 262p.

Gontijo, R. and Cunha, F., 2015. "Dynamic numerical simulations of magnetically interacting suspensions in creeping flow". *Powder technology*, Vol. 279, pp. 146–165.

Gontijo, R. and Cunha, F., 2017. "Numerical simulations of magnetic suspensions with hydrodynamic and dipole-dipole magnetic interactions". *Phys. Fluids*, Vol. 29, No. 6, p. 062004.

Huang, C., Yao, J., Zhang, T., Chen, Y., Jiang, H. and Li, D., 2017. "Damping applications of ferrofluids: a review". *Journal of Magnetics*, Vol. 22, No. 1, pp. 109–121.

Liu, X., Zhang, Y., Wang, Y., Zhu, W., Li, G., Ma, X., Zhang, Y., Chen, S., Tiwari, S., Shi, K. *et al.*, 2020. "Comprehensive understanding of magnetic hyperthermia for improving antitumor therapeutic efficacy". *Theranostics*, Vol. 10, No. 8, p. 3793.

Odenbach, S., 2009. *Colloidal magnetic fluids: basics, development and application of ferrofluids*, Vol. 763. Springer.

Rosensweig, R.E., 2002. "Heating magnetic fluid with alternating magnetic field". *J. M. M. M.*, Vol. 252, pp. 370–374.

Savi, M.A., 2006. *Dinâmica não-linear e caos*. Editora E-papers.

Silva, A.C.d., Oliveira, T.R., Mamani, J.B., Malheiros, S.M.F., Pavon, L.F., Sibov, T.T., Amaro, E. and Gamarra, L.F., 2010. "Magnetohyperthermia for treatment of gliomas: experimental and clinical studies". *Einstein (São Paulo)*, Vol. 8, pp. 361–367.

Stephen, P.S., 1965. "Low viscosity magnetic fluid obtained by the colloidal suspension of magnetic particles". US Patent 3,215,572.

Thiesen, B. and Jordan, A., 2008. "Clinical applications of magnetic nanoparticles for hyperthermia". *International journal of hyperthermia*, Vol. 24, No. 6, pp. 467–474.

Uhlmann, E., Schäper, E. and Bayat, N., 2002. "Einrichtung zum positionieren eines körpers". *German patent DE*, Vol. 102, No. 44867, p. 394.

7. RESPONSIBILITY NOTICE

The authors are solely responsible for the printed material included in this paper.